Autonomous Ocean Turbulence Measurements Using Shear Probes on a Moored Instrument

ILKER FER AND MOSTAFA BAKHODAY PASKYABI

Geophysical Institute, University of Bergen, Bergen, Norway

(Manuscript received 2 May 2013, in final form 29 August 2013)

ABSTRACT

An internally recording, autonomous instrument has been tested for measurements of ocean turbulence from a mooring line. Measurements were made at a single level in the water column, but for an extended period of time, at a predetermined duty cycle. The instrument is designed to measure, independently, in two different parts of the turbulence wavenumber spectrum: eddy correlation measurements in the inertial subrange and small-scale shear and temperature gradient measurements in the dissipation subrange using shear probes and fast-response thermistors. For the deployment reported here, the instrument is located in the wave-affected layer, and only the dissipation subrange from the shear probes can be confidently utilized for turbulence measurements. The velocity spectra in the inertial subrange are severely contaminated by platform motion and noise, and the dissipation range of the temperature gradient spectrum is not satisfactorily resolved. The shear spectra are found to be relatively free of contamination in the 1–20-Hz frequency range and are used for dissipation rate calculations. The quality of the measurements is constrained by the angle of attack and the magnitude of mean flow relative to the wave oscillatory velocities. Dissipation rates are consistent with a scaling expected from breaking long waves, when background shear is weak, and are elevated when the gradient Richardson number is small, consistent with additional turbulence production by shear. While limited to a single depth, the instrument makes it possible to collect time series for 3 weeks continuously or for 3 months at a 25% duty cycle.

1. Introduction

The measurements of turbulence and mixing in the open ocean are typically limited to intensive surveys of a few weeks' duration conducted from research vessels. Although undersampled and sporadic in time and space, such observations have contributed significantly to improving our understanding of the ocean mixing processes (Thorpe 2005). Measurements for extended periods, however, are needed to resolve the critical role of ocean mixing on regional and larger-scale ocean circulation dynamics (Wunsch and Ferrari 2004). Time series of turbulent fluxes measured by self-recording instruments at several levels for several months' duration in a mooring line can help to link the mixing to larger scales (Moum and Nash 2009). In the following, microstructure is used for fluctuations associated with small-scale turbulence, whereas fine structure is associated with inhomogeneities related to stratification.

Conventionally, ocean microstructure is measured by airfoil shear probes and/or fast thermistors sampling the dissipation subrange of the turbulence spectrum. Fluxes are then inferred from shear, conductivity, or temperature variances resolved at dissipative scales by sensors on profiling or towed instruments, or autonomous underwater vessels. A detailed review on ocean microstructure measurements is given by Lueck et al. (2002). Using sea ice as a stable platform, oceanic turbulent flux measurements can be made by eddy-correlation methods in the underice boundary layer; see McPhee (2008) for a review. Such measurements require the sampling of velocity and temperature fluctuations at approximately the same measurement volume and have been made from drifting ice (e.g., McPhee et al. 1987; McPhee 1992) or from fast ice (e.g., Fer and Widell 2007). Near the surface of the upper ocean, however, the wave orbital velocities and the platform motion, which typically dominate the turbulent velocity fluctuations at the scales containing fluxes, must be accounted for.

Denotes Open Access content.

Corresponding author address: Ilker Fer, Geophysical Institute, University of Bergen, Allégaten 70, 5007 Bergen, Norway.
E-mail: ilker.fer@gfi.uib.no

DOI: 10.1175/JTECH-D-13-00096.1

All types of turbulence measurements typically assume that the turbulent eddies are frozen and advect past the sensors at a known or measured mean speed. For measurements from profiling, towed, or propelled instruments, this speed is well defined as the sink, rise, or tow speed of the instrument through the water. A moored instrument, on the other hand, relies upon ambient current to advect the turbulent eddies past its sensors.

The first attempt to conduct autonomous moored microstructure measurements by use of shear probes and fast temperature sensors was reported by Lueck et al. (1997). The instrument burst sampled for 128 s every 5 min, but due to technical limitations could only store reduced data such as band-averaged spectra and statistical parameters for each burst in addition to a one unprocessed dataset every 6 h. With today's technology and data storage capacity, several months of raw data sampling and storage are possible. The dissipation rate of turbulent kinetic energy (TKE) per unit mass (ε) could be measured to a noise level of $\approx 10^{-10}\,\mathrm{W\,kg^{-1}}$ for a mean flow of $0.1\,\mathrm{m\,s^{-1}}$. More recently, extended mixing measurements were made from a mooring by using a string of temperature microstructure recorders (χpod) sampling at several levels (Moum and Nash 2009). These instruments do not contain shear probes and measure time series of dissipation of temperature variance (χ) and inferred ε, which compared well with historical data from the same location. Zhang and Moum (2010) used the same dataset to obtain independent estimates of χ and ε from the low wavenumber portion (inertial-convective subrange) of the temperature gradient spectra. The vertical motion induced by the pumping of the surface buoy contaminated the spectra, which could be removed using independent vertical acceleration measurements. A more direct comparison of χpod data with simultaneous microstructure profiles was reported in Perlin and Moum (2012). When averaged over a 15-day period, the values of dissipation rate of temperature variance and TKE generally agreed within 95% of the bootstrap confidence limits; however, significant differences on the average values were reported on 2-day time scales, presumably due to the natural variability and uncertainties in the relative depth of measurements in regions where turbulence gradients were strong.

Here, we report microstructure observations from a moored instrument deployed in the wave-affected upper layer of the water column. Near-surface turbulence measurements are challenging; platform motions contaminate the time series and the surface wave orbital velocity fluctuations are several orders of magnitude larger than the turbulent velocity fluctuations. In our dataset, the velocity spectra are noisy and the inertial subrange is severely contaminated; furthermore, the roll off of the temperature gradient spectrum is not resolved. We therefore concentrate on the shear probe measurements in this paper. The components of the instruments and the description of our methods in processing the shear probe data are presented and discussed. Our work builds on the previous studies in that, compared to Lueck et al. (1997), longer periods of measurements are possible for storing raw data and using commercially available off-the-shelf instruments and components, and compared to Moum and Nash (2009), dissipation measurements are made using shear probes. While the deployment reported here is in the upper layer of the water column, a project addressing wave-induced turbulence, the instrument can be deployed at any desired depth in the water column. Successful deployments have been made, following this first deployment, for 2.5 months in the upper ocean on the Norwegian continental shelf covering periods of two storms, and for 2 weeks in the turbulent dense gravity current plume of the Faroe Bank Channel overflow at 850-m depth about 100 m from the seabed. The analysis of these unique datasets, which could not be collected by other means, is in progress and the knowledge gained emphasizes the strength of moored mixing measurements.

The outline of this paper is as follows. The instrument, its components, the coordinate system, and the sampling details are given in section 2. The site and environmental forcing during the experiment are described in section 3. The subsequent section on data processing includes details on the platform motion, processing of the shear probe data, angle of attack calculations, and the quality screening applied to the dataset. In section 5 the results are presented and discussed, including frequency spectra from three selected 15-min periods, wave orbital velocities, and noise level for shear measurements. Using the entire dataset, shear spectra averaged in varying levels of turbulence and the time series of resulting dissipation rate calculations are presented and discussed in relation to external forcing. Concluding remarks are finally given in section 6.

2. Instrument

a. Components

The instrument, Moored Autonomous Turbulence System (MATS) (Fig. 1), is an ocean turbulence measurement system designed in close collaboration with Rockland Scientific International (RSI, Canada) to collect microstructure time series at a fixed level. MATS consists of a main body platform, a modified RSI turbulence package MicroRider-1000LP (hereafter MicroRider), a three-component Nortek Vector acoustic Doppler velocimeter (ADV, hereafter Vector), and a pair of rechargeable

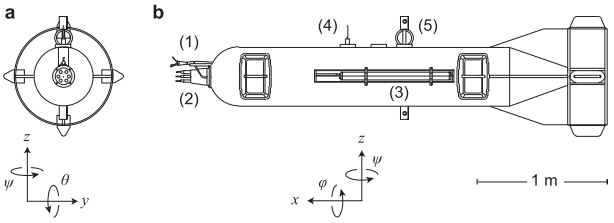

FIG. 1. MATS components and the coordinate system (to scale). (a) Front view. (b) Side view showing 1) the vector, 2) the nose cone of the MicroRider with turbulence sensors, 3) one of the two lithium-ion battery packs, 4) Argos beacon, and 5) lifting arbor. The positive sense of rotation for pitch (θ), roll (ϕ), and yaw (ψ) is also shown.

lithium-ion battery packs. The assembled instrument weighs approximately 290 kg and has a buoyancy equivalent to 160 kg. It has an overall length of 3 m, and a midbody diameter of 46 cm. The entire system is powered by the battery packs, each rated for 40 Ah at 14.8 Vdc, giving an estimated operating time of 500 h. With a 25% duty cycle—for example, 15-min bust sampling every hour—MATS can sample 20 GB of data for about 85 days.

The platform is a low-drag buoy, StableMoor 400 from Flotation Technologies, specifically designed for high-current applications. The StableMoor has a nominal drag coefficient of 0.3 and minimizes mooring inclination and excursions. The buoy, depth rated to 750 m, is custom modified to fit the turbulence instruments and the battery packs. The 46-cm diameter of the main body is tapered to a 15-cm diameter at the nose section housing the turbulence sensors. The diameter increases to 76 cm at the fletching at the rear, which provides aerodynamic stabilization. The buoy can be used as the upper buoyancy element or can be integrated at the desired depth in a mooring line. A swivel allows the instrument to align with the current, pointing the sensors toward the undisturbed, free flow.

The MicroRider is a modified version of the standard RSI low-power MicroRider. It is neutrally buoyant. In addition to the standard suite of sensors including two airfoil shear probes, two fast-response FP07 thermistors, a pressure transducer, a two-axis vibration sensor (a pair of piezo-accelerometers), and a high-accuracy dual-axis inclinometer (ADIS 16209, pitch and roll angles accurate to 0.1°), the MiroRider is fitted with a low-power six-axis motion sensor (O-Navi, Gyrocube 3F), and an integrated low-power three-axis magnetic field sensing module (MicroMag3). The Gyrocube3F integrates three angular rate gyros and three accelerometers in a triaxial orthogonal configuration. The main pressure case contains the electronics and the data acquisition computer (Persistor CF2), together with the magnetometer and the motion sensor.

The Vector is a 6-MHz acoustic velocimeter measuring the 3D velocity fluctuations in water. All turbulence sensors of the MicroRider and the sensor head of the Vector protrude horizontally from the nose of the buoy pointing into the mean flow. No probe guard is installed. The sensor head of the Vector is rigidly fixed to the buoy, as close as possible to the MicroRider sensors, such that the temperature and the 3D velocity components are sampled at approximately the same measurement volume. The tip of the turbulence sensors is about 25 cm from the nose of the buoy and the measurement volume of the Vector is approximately another 5 cm farther.

b. Coordinate system

The shear probes are mounted orthogonal to each other to measure the $\partial w/\partial x$ and $\partial v/\partial x$ shear components. A right-handed Cartesian coordinate system is used throughout with x pointing forward along the major axis of the instrument, y pointing to the port side of the instrument, and z upward (Fig. 1). Accordingly, pitch (θ, rotation about the y axis) is positive when the nose is down, roll (ϕ, rotation about the x axis) is positive when the instrument rolls port side up, and yaw (ψ, rotation about the z axis) is positive counterclockwise. Note that in this body frame, for nonzero values of pitch and roll, the vertical axis is not aligned with the gravity (g).

c. Sampling

The power supply board of the MicroRider is configured in cyclic sampling, allowing the instrument to wake up at predetermined intervals (duty cycle). For the present study, we used a duty cycle of 15 min on and 1 min off (section 3a). Sampling rate is set to 512 Hz on all turbulence channels (vibration, shear, and temperature gradient) and 64 Hz for the other channels including the compass, the Vector, and the motion pack. The MicroRider also samples the signal plus signal derivative on the thermistor and pressure transducer, and the derivative for shear signals allowing high-resolution measurements (Mudge and Lueck 1994). Data are recorded on a 16-GB CompactFlash memory card.

The signal conditioning board of the MicroRider is modified to record the analog output signal from the Gyrocube and the Vector. Because the Gyrocube is an analog device, the motion sensor dataset is synchronized with the microstructure measurements. The Vector's digital output is first converted to analog signal, and the internal harness of the Vector is rewired to enable the analog signal outputs to the MicroRider, where the data are recorded. This does not degrade the output and ensures that the Vector is synchronized. Interfacing with the MicroRider also allows for controlling the Vector for the chosen duty cycle. The Vector samples in instrument

coordinates at a 16-Hz rate and drains power from the MATS battery packs. The MicroRider, however, stores data from the Vector at 64 Hz, that is, records redundant samples. After reading and converting the Vector velocity data from the MicroRider, the velocity measurements are decimated to 16 Hz prior to analysis.

The Vector emits significant electromagnetic interference at a 30-MHz frequency, which is picked up by the thermistor circuits. This noise is heavily attenuated when the instrument is immersed in water. Initial tests showed that the standard deviation on the shear probe and thermistor channels (with dummy probes) increased to 20 times the nominal levels when the Vector was running. The noise is reduced to normal levels after installing a suppression circuit inside the Vector, and further using ferrite chokes and nonpolarized (NPO) ceramic capacitors on the power lines.

d. Application

In favorable conditions, MATS allows for measurements using two independent methods, sampling different parts of the turbulence spectrum: eddy correlation measurements of turbulent momentum flux and heat flux sampled in the energy containing a near-inertial subrange, and dissipation rate measurements in the dissipation subrange (again, using two independent methods using shear probes, and temperature gradient data from FP07s). Records from the accelerometers and the 6D motion sensor allow for applying necessary corrections for the platform motion. An example of calculations for compensating for package motion of χpod using a motion sensor with three linear accelerometers and three angular rate sensors can be found in the appendixes of Perlin and Moum (2012). The present dataset in the wave-affected upper ocean, however, is not suitable for measurements in the inertial subrange of the velocity spectrum or the dissipation subrange of the temperature gradient spectrum. The surface wave orbital velocity fluctuations severely contaminate the inertial subrange, and even though motion correction may be possible using the available data, the velocity spectra are dominated by noise at frequencies as low as 0.3 Hz (see section 5a). Because of the elevated levels of turbulence in the upper ocean and the limited time response of the FP07 sensor, the temperature gradient spectrum cannot be resolved satisfactorily. The time response corrections become too large and uncertain at wavenumbers where most of the temperature gradient variance occurs. Measurements of the dissipation rate of temperature variance (χ) become uncertain. As a consequence, only results from the shear probes are reported in this paper.

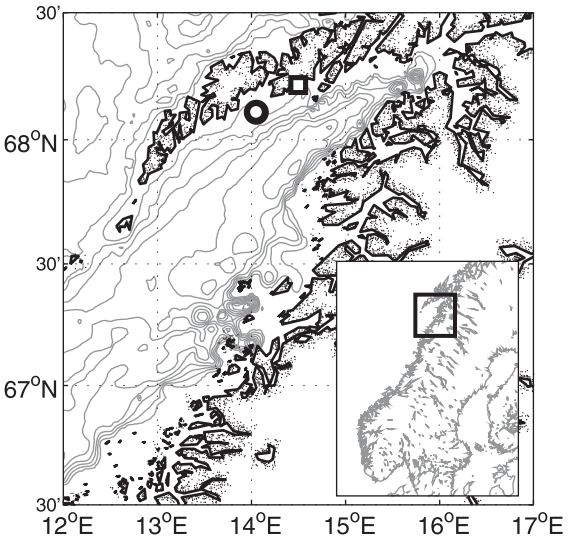

FIG. 2. Deployment site, together with the isobaths at 50-m intervals. The position of MATS (bullet) and the tide gauge at Kabelvåg (rectangle) are shown. The borders of the detailed map are marked in the inset showing the location in Norway.

3. Experiment

a. Site and deployment

MATS was deployed in Vestfjorden in northern Norway (Fig. 2) at 1010 UTC 9 April 2011 at 68°6.57′N, 14°2.9′E in 128-m-deep water. The instrument was recovered at 0700 UTC 13 April during the same cruise of the Research Vessel *Johan Hjort*. The duty cycle of sampling was set to 15 min on and 1 min off. While the average time between the start of subsequent segments is 16 min (within ±1 s), each segment is 14.5 min long due to initializing of data acquisition and file bookkeeping.

The mooring line of MATS was also instrumented with a 300-kHz RD Instruments (RDI) acoustic Doppler current profiler (ADCP) at 70 m from the surface, and two Sea-Bird Electronics (SBE) MicroCATs, one at immediately below MATS and the other 5 m deeper at about 18-m depth (Fig. 3). MATS was located at about 12-m depth, and the mean and standard deviation of the pressure record for the duration of the deployment was 12.7 ± 0.5 dbar. The average pressure recorded by the MicroCATs was 12.9 and 18.2 dbar, respectively. MATS sampled 15-min bursts every 16 min. The MicroCATs sampled every 10 s. The ADCP was set to average 120 ensembles of profiles every 1 min using a 2-m vertical cell size, giving a single ping standard deviation of 0.6 cm s^{-1}. Both the pitch and roll of the ADCP were always less than 1° with root-mean-square (rms) values of 0.6 and 0.5°, respectively.

Ancillary data include standard meteorological measurements at 1-min intervals from the ship's mast at approximately 20-m height, and hourly water-level

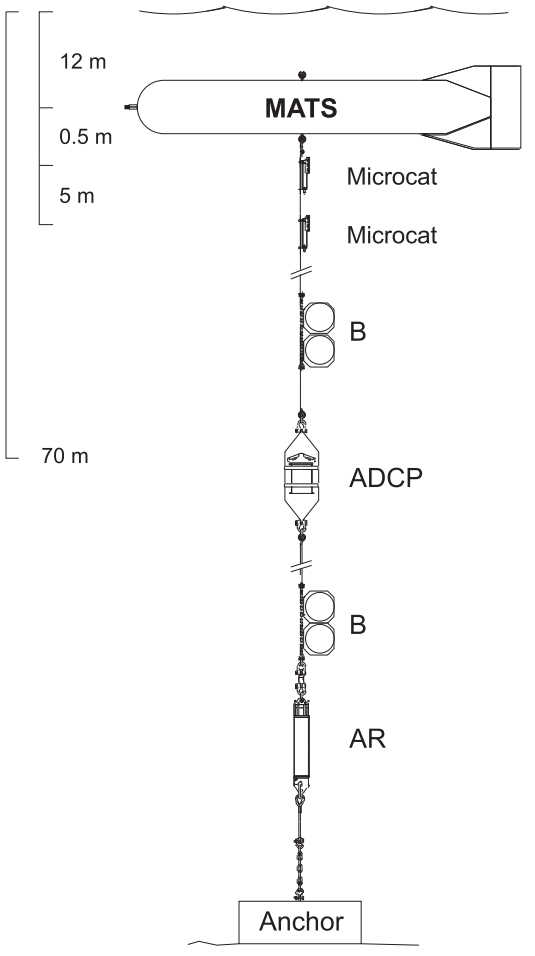

FIG. 3. Sketch of the MATS mooring as deployed in Vestfjorden (not to scale). The 116-m-long mooring line comprises an acoustic release (AR), a 300-kHz ADCP, buoyancy elements (B, a couple of 17-in. glass spheres each) above the AR and the ADCP, two MicroCATS, and MATS at the top. The buoyancy elements above the ADCP are 5 m above the transducers and do not block the acoustic beams.

measurements obtained from the Norwegian Hydrographic Service tide gauge at Kabelvåg at 68°13′N, 14°30′E (Fig. 2). Because of a technical problem, the ship had to leave the experiment site and was moored near Kabelvåg between 1500 UTC 11 April and 1100 UTC 12 April. During this period (marked by gray in Fig. 4a) wind measurements are not representative of the MATS site. For the remaining part of the MATS deployment, the average distance of the ship to the MATS position was about 4 km.

b. Environmental forcing

Vestfjorden is a wide fjord exposed to a long period swell from the Norwegian Sea from the southwest and is dominated by a typical cyclonic circulation. A description of the meteorological, oceanographic, and wave conditions at the site, together with other field work conducted during the cruise, is given in Röhrs et al. (2012). Prior to the deployment of MATS, on 9 April, westerly winds exceeded 12 m s^{-1}. The wind then ceased to calm conditions before it picked up on midday 10 April, reaching 14 m s^{-1}. The evolution of the wind speed and direction can be seen in Fig. 4a. Water-level fluctuations are dominated by the semidiurnal tides. The pressure record from MATS agrees perfectly with the water-level fluctuations measured at Kavelvåg, suggesting insignificant mooring knockdown in response to currents during the deployment. The rms deviation between the water level and the MATS pressure record anomaly was 0.04 dbar with a maximum value of 0.08 dbar. Wave spectra are inferred from the pressure sensor of MATS as described by Bakhoday Paskyabi and Fer (2013). Significant wave heights in excess of 2 m were recorded during the first hours of the deployment and also on 10 April, following the onset of the wind.

Observed current, averaged in the depth range 10–70 m (of the 128-m total depth) ensonified by the ADCP and over the duration of the deployment, is 7.2 cm s^{-1} from about 250° measured from north, approximately parallel to the local isobath orientation. The mean current, however, is superimposed on a significant near-inertial period variability with amplitude comparable to the mean flow. The near-inertial variability is composed of the semidiurnal tidal currents and the inertial waves as a result of wind forcing, particularly evident as a slanted, upward-propagating phase distribution after the wind event on 10 April. Contours of the baroclinic velocity, approximated by removing the depth-averaged current from the observed profiles, show a variability of ±20 cm s^{-1}.

c. Platform behavior

Pitch and roll were small and relatively constant in time with average values of $\theta = -2.7 \pm 0.3°$ and $\phi = 1.2 \pm 0.1°$, respectively (see Fig. 5). The bearing of the instrument is compared to the mean ambient current direction measured by the ADCP at the depth of MATS. Throughout the observation period, the instrument responded to the currents, ranging from 1 to 22 cm s^{-1}, and was aligned with the mean current, opposing the incoming flow, to within 9° ± 11° (Fig. 5). For 50% of the observations, the difference between the current direction and the negative bearing was less than 10°. At the level of MATS, the average horizontal speed measured by the ADCP (at 12 m) was 12.8 ± 5 cm s^{-1}. This is identical, within the measurement uncertainties, to 12.7 ± 4 cm s^{-1} measured by the Vector on MATS.

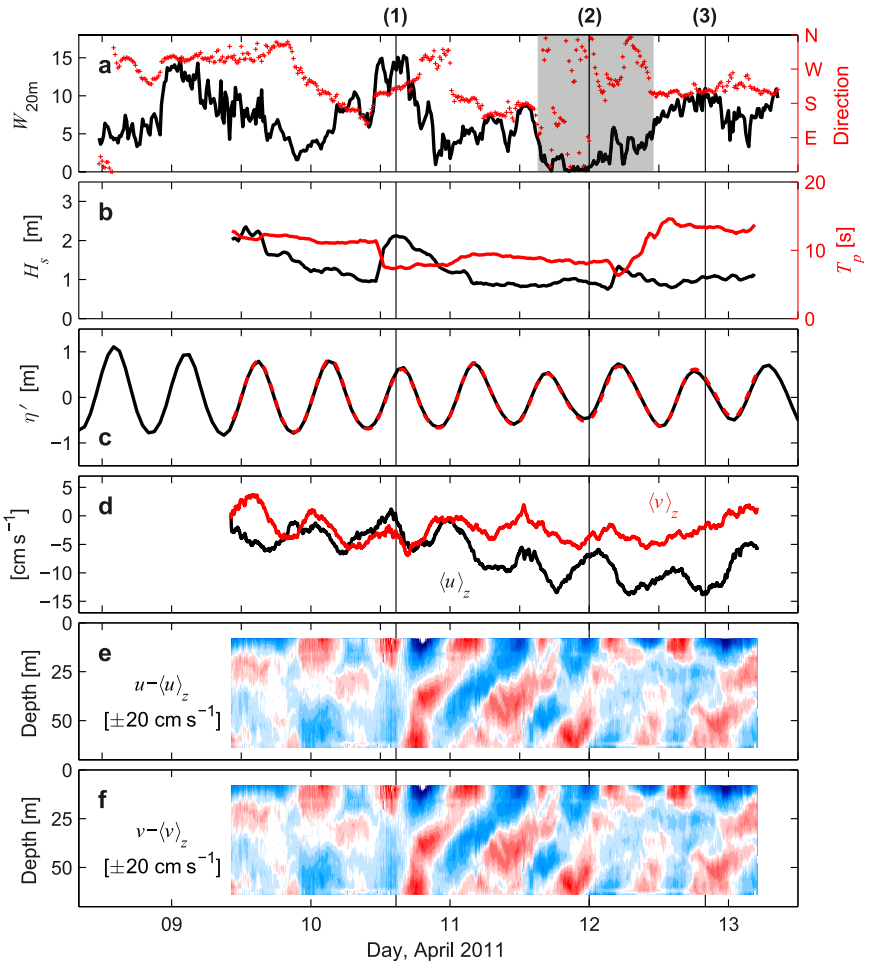

FIG. 4. Environmental forcing during the deployment. Time series of (a) wind speed (black) and direction (red) measured at 20-m height from the ship's meteorological mast; (b) significant wave height H_s (black) and the peak wave period T_p (red) inferred from the MATS pressure measurements; (c) water-level anomalies (black) and pressure anomalies (red, dashed) measured at Kabelvåg and at MATS, respectively; (d) depth-averaged east $\langle u \rangle_z$ (black) and north $\langle v \rangle_z$ (red) components of the velocity measured by the RDI ADCP; and depth-time distribution of (e) east and (f) north components of the velocity after removing the depth average. Anomalies in (c) are obtained by linearly detrending each dataset in the MATS observation period. During the gray-shaded period in (a) the ship was moored near Kabelvåg and the wind measurements are not reliable. The vertical lines mark the three segments for which the spectra are shown.

4. Data processing

a. Platform motion

The accelerations measured by the accelerometers include an inertial component and a gravitational component due to tilting of the instrument. In the right-handed body-coordinate frame adopted here, measured accelerations are

$$\begin{aligned} a_x &= a_{x-g} + a_{x-i} = -g\sin\theta + \ddot{\mathbf{r}}_x \\ a_y &= a_{y-g} + a_{y-i} = g\sin\phi\cos\theta + \ddot{\mathbf{r}}_y \\ a_z &= a_{z-g} + a_{z-i} = -g\cos\theta\cos\phi + \ddot{\mathbf{r}}_z, \end{aligned} \tag{1}$$

where $\ddot{\mathbf{r}}_i$ is the linear acceleration and the double dots indicate second derivatives of the platform displacement vector $\mathbf{r}_i$. The pitch and roll signals can be unambiguously separated from the inertial accelerations using the angular rate sensors. Roll (ϕ), pitch (θ), and yaw (ψ) can be obtained by integrating $\ddot{\mathbf{r}}_x$, $\ddot{\mathbf{r}}_y$, and $\ddot{\mathbf{r}}_z$, respectively, measured by the angular rate sensors. As a result of the inherent drift in the rate sensors, however, the practical approach is to integrate the high-pass filtered rate signal and add this to the low-pass filtered reference angles (complementary filtering; see, e.g., Edson et al. 1998). The time constant (τ) for filtering depends on the behavior of the platform and

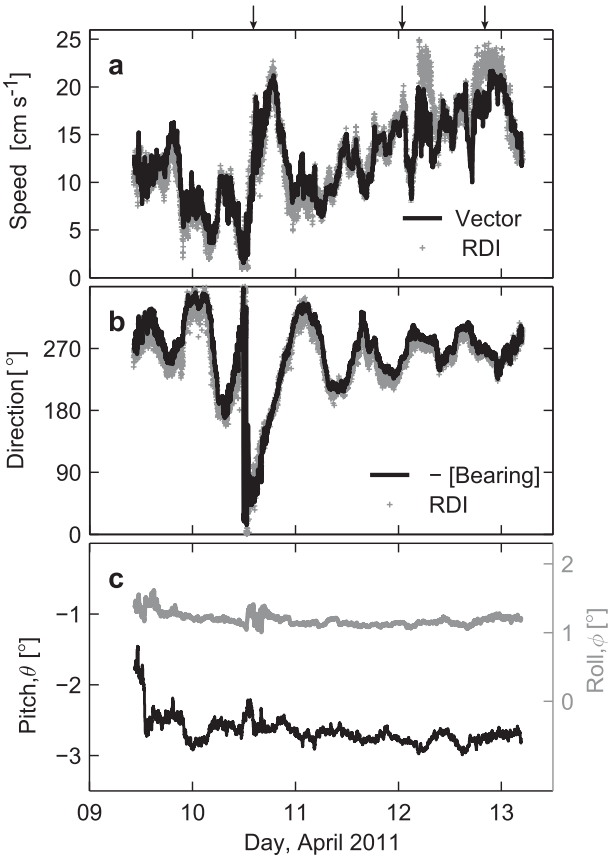

FIG. 5. (a) Horizontal speed measured by the vector on MATS (black) and by the ADCP at the bin centered at 12 m, closest to the depth of MATS (gray). (b) Direction of the current measured the ADCP at 12 m (gray) and the negative bearing of MATS (black) measured by the magnetometer. (c) Pitch and roll measured by the motion sensor. Arrows mark the time of the three selected segments.

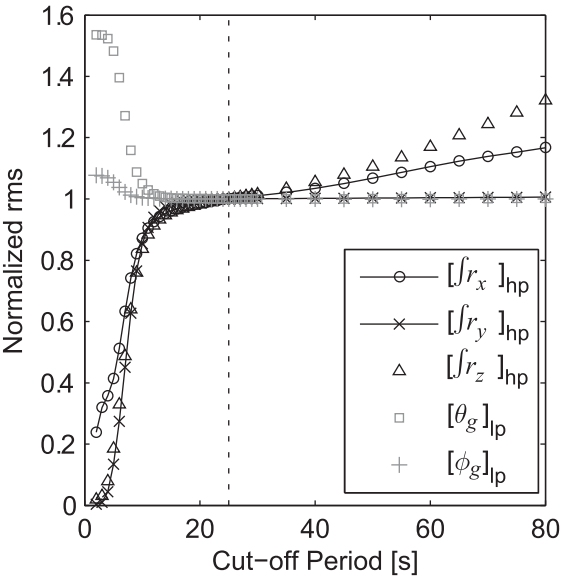

FIG. 6. Influence of the filter cutoff period on the statistics of high-pass integrated rate signals, and the low-pass pitch and roll inferred from the acceleration.

the environmental forcing. To determine τ, results from filter cutoff periods between 1 and 80 s are tested (Fig. 6). The evolution of the rms values of relevant parameters, such as the high-passed integrated rate signal and the low-passed gravitational component of the measured acceleration, suggests that $\tau = 25$ s separates the wave-induced band that dominates the acceleration spectra in 3–10-s time scales from low-frequency tilts.

b. Shear probes

Before converting the raw data from the MicroRider into physical units, the pressure and thermistor channels recording the signal plus signal derivative are deconvolved to obtain high-resolution pressure and temperature records. The shear probe data voltage output is converted to shear using the known electronic constants, the sensitivity of the shear probe, and the flow past the sensors measured by the Vector. For the latter, a smooth 3D velocity field, low-pass filtered with a 2-s cutoff, is interpolated to 512 Hz. The smoothing time is based on the low-frequency end of the shear spectra portion (1–20 Hz) chosen for obtaining shear variance uncontaminated by wave motion and noise. The smoothed velocity ensures that the highly variable flow near the surface (due to wave orbital velocities) is accounted for as the flow advects past the sensors.

Each 15-min burst is segmented into half-overlapping 60-s-long portions for spectral analysis. An FFT length corresponding to 15 s is chosen, and each 15-s segment is detrended and Hanning windowed before calculating the spectra. The shear probe signal coherent with the accelerometer data (from the two-axis vibration sensors) are removed using the method outlined in Goodman et al. (2006). Dissipation rates are calculated from both the clean and the original shear spectra for further inspection.

The frequency domain shear spectra $\Phi(f)$ are converted into the wavenumber domain using Taylor's frozen turbulence hypothesis and using the 2-s smoothed flow averaged over the 60-s windows, using $\Phi(k) = V\Phi(f)$ and $k = f/V$. The mean flow (V) does not change substantially between the 15-s segments in each 60-s window. The portion of the shear spectra between 1 and 20 Hz are extracted to obtain the dissipation rate. For the typical mean flow speeds of $V = 0.2\,\mathrm{m\,s^{-1}}$ during the experiment, this range corresponds to 5–100 cycles per meter (cpm). Reprocessing the entire dataset, using the portion of the spectra between 0.5 and 40 Hz, leads to

2.7 (±1.3) times larger dissipation rates. The wavenumber spectra are then corrected for the shear probe's limited spatial response with a cutoff wavenumber of 48 cpm.

The dissipation rate of TKE for each segment is calculated by assuming isotropic turbulence, and by integrating the wavenumber spectrum as

$$\varepsilon_j = \frac{15}{2}\nu\overline{\left(\frac{\partial u_j}{\partial x}\right)^2} = \frac{15}{2}\nu\int_{k_l}^{k_u}\Psi(k)\,dk, \qquad (2)$$

where j (=1, 2) identifies the shear probe number ($u_1 = w$ and $u_2 = v$); ν is the kinematic viscosity, which is a function of the local water temperature; and the overbar denotes a spatial average. Integration is carried out similar to that described in appendix A of Moum et al. (1995). The empirical model for the turbulence spectrum determined by Nasmyth is used to set the lower (k_l) and upper (k_u) integration limits of the spectrum and to correct for the variance in the unresolved portions of the spectrum. The Nasmyth form indicates that 90% of the variance is resolved by integrating to $0.5k_K$, where $k_K = (2\pi)^{-1}(\varepsilon/\nu^3)^{1/4}$ is the Kolmogorov wavenumber (cpm). An initial estimate of ε is made by integrating the normalized wavenumber range $0.015 < k/k_K < 0.05$, and then iteratively adjusting the integration band. Our integration band is limited by the chosen range of frequency band (1–20 Hz). For low dissipation rates of about $10^{-9}\,\mathrm{W\,kg^{-1}}$, the spectra rolls off at about 5 cpm, and the lower limit of 1 Hz corresponding to about 5 cpm (for $V = 0.2\,\mathrm{m\,s^{-1}}$) is not adequate. Typical dissipation rates in the upper ocean, however, are larger and the spectra roll off at larger wavenumbers. Also note that the restricted frequency band here is special for the wave-affected layer measurements, and no such restriction is necessary for deeper measurements (i.e., lower wavenumbers can be adequately resolved). For the upper limit, the integration is stopped at 50 cpm when $0.5k_K > 50$ cpm.

c. Angle of attack

The shear probes use the potential flow theory to measure the hydrodynamic lift force induced by the turbulent flow. This principal is violated and the probes cannot respond linearly to cross-stream velocity fluctuations when the angle of attack (AOA) of the flow relative to the total flow speed V exceeds about ±20° (Osborn and Crawford 1980).

The Vector current meter is rigidly fixed to the instrument and one axis is always parallel to the shaft of the shear probes, allowing for reliable estimates of AOA. The AOA for time scales longer than the lowest frequency used to estimate the dissipation rate can be large and highly variable as a result of wave orbital velocities in the surface gravity wave frequency band. The dissipation rate measurements are obtained by integrating the shear spectra starting from approximately 1 Hz. For our purpose, a good estimate of the AOA felt by the shear probes is thus at the time scale corresponding to 1 Hz. We attempt to estimate the relevant AOA for the shear probe measurements in the rms sense from the spectral content of the velocity time series, in the frequency band from 0.5 to 2 Hz (a factor-of-2 window centered at a 1-s period). A low-frequency AOA and a high-frequency AOA are estimated from the 2-s low-passed velocity measurements and from the velocity spectra, respectively, as follows:

$$\begin{aligned}\mathrm{AOA_{LF}} &= \arctan(w_{\mathrm{lp}}/\langle u\rangle)\\ \mathrm{AOA_{HF}} &= \arctan[w_{1s}/(\langle u\rangle + u_{1s})],\end{aligned} \qquad (3)$$

where $\langle u\rangle$ is the segment-average along-axis velocity; w_{lp} is the 2-s low-passed vertical velocity; and w_{1s} is the vertical velocity, in the rms sense, obtained as the square root of the integral of the spectrum in the frequency band 0.5–2 Hz. The instantaneous AOA cannot be calculated from the spectral content; a rough estimate, however, can be made. For a Gaussian distribution, the peak value is approximately 3 times larger than the rms value (Lueck et al. 1997)—that is, the instantaneous value is at most 3 times the rms value. For turbulent flows with a skewed distribution, larger peak-to-rms ratios may occur; nevertheless, we assume that the $|\mathrm{AOA}| < 20°$ condition can be replaced by $|\mathrm{AOA_{HF}}| < 7°$. Removing the along-axis velocity u spectral contribution increases $\mathrm{AOA_{HF}}$ by less than 0.1° on the average, occasionally up to 1° between 1100 and 1300 UTC on 10 April.

A good estimate (percentage wise) of instantaneous angle of attack at scales resolved by ADV, $\mathrm{AOA_{PG}}$, is calculated as the percent of occurrence with $\mathrm{AOA_{LF}} < 20°$ within each 15-min burst. $\mathrm{AOA_{PG}}$ varies between 0% and 75%; near-zero values occur during the windy period with large waves on 10 April, noon (Fig. 7). Typically, the rms over 15 min of instantaneous $\mathrm{AOA_{LF}}$ increases above 40° when $H_s > 1.5$ m, and $\mathrm{AOA_{PG}}$ is consistently less than 40%. In the latter half of the record, peak-to-peak $\mathrm{AOA_{LF}}$ varies between ±40° with an average rms value of 33° ± 4° (Fig. 7c). As expected, AOA inferred from the low-passed field is large and variable as a result of the wave orbital velocities in the 0.05–1-Hz frequency range (periods from 20 to 1 s). Because we use only the high-frequency portion (>1 Hz) of the shear spectra, this is not representative of the AOA at time scales used to estimate the dissipation rate, and

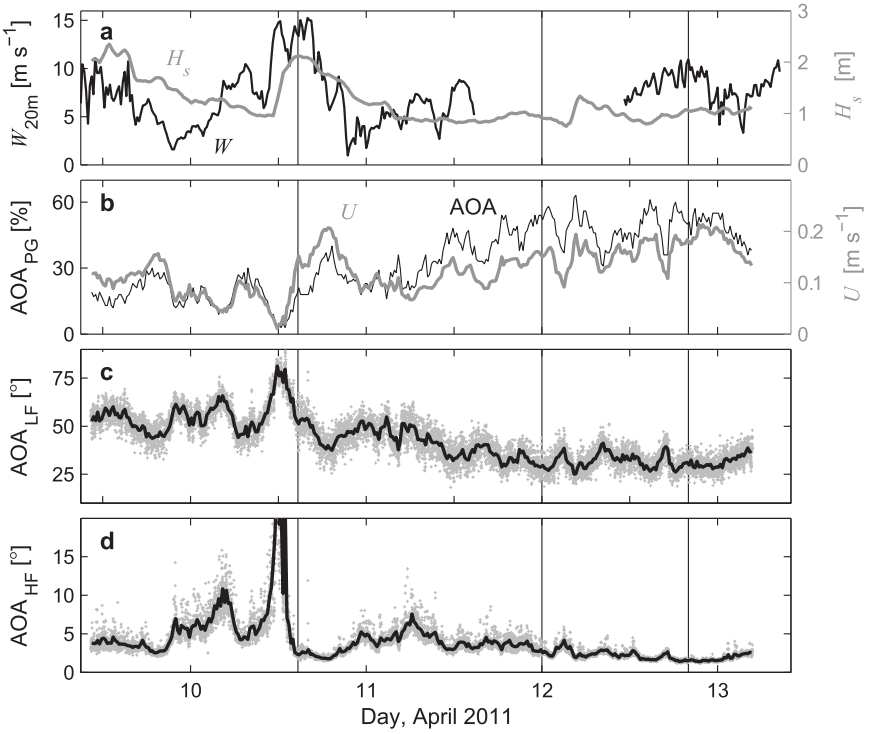

FIG. 7. Summary of the inferred AOA throughout the deployment. Selected environmental forcing parameters are also shown for reference. (a) Wind speed W_{20m} and significant wave height H_s; (b) horizontal flow U and percent good of AOA AOA_{PG}; (c) low-frequency AOA_{LF}; and (d) high-frequency AOA_{HF} estimates of AOA. Wind speed measurements during the period when the ship was moored near land are excluded. Vertical lines mark the chosen three segments for which the spectra are shown.

AOA_{HF} (Fig. 7d) can be used for the quality screening of shear probe measurements. The average AOA_{HF} is 3.6° ± 1.7° when the windy period (noon, 10 April) is excluded.

d. Quality screening

Dissipation rate measurements of acceptable quality are limited to a (small) subset of environmental conditions. In addition to the AOA, which is a crucial constraint on the quality of the shear probe data, the applicability of Taylor's hypothesis must be verified, especially when the wave orbital velocities and the mean flow are of comparable magnitude. At times when the mean current is not strong enough, the oscillating motions due to surface waves advect turbulent eddies (both natural and artificial due to wake of the instrument) back to the vicinity of the shear probes. The measured velocity spectra, compared to the wave orbital velocities expected from the linear wave theory, are discussed in section 5b. The typical surface gravity wave band covers periods from 20 to 1 s. Here, we estimate the (rms) magnitude of wave-induced motion, for each 60-s segment, by integrating the velocity spectra in the frequency band corresponding to 20 to 1 s:

$$\mathbf{u}^2_{\text{wave}} = \int_{0.05}^{1} [\Psi_u(f) + \Psi_v(f) + \Psi_w(f)]\, df. \qquad (4)$$

The ratio R of the mean flow to wave-induced flow is then estimated as

$$R = |\mathbf{u}|/|\mathbf{u}_{\text{wave}}|, \qquad (5)$$

where $\mathbf{u}$ is the mean flow measured by the Vector. Ideally, to satisfy Taylor's hypothesis one would require $R \gg 1$; however, in our dataset $R < 3$ at all times and $R > 2$ for only 6% of the record. A scatterplot of R against ε shows that ε spuriously increases, abruptly, around $R \approx 1.1$ (not shown). A data segment is therefore ignored when $R < 1.5$ or when $|AOA_{HF}| > 7°$. In total, 54% of the segments satisfying these criteria are excluded. Large values of AOA were associated with $R < 1.5$ at all times. In total 5118 segments had $R < 1.5$, of which 791 had $|AOA| > 7°$ and 29 showed substantial roll (mean roll greater than 2° or rms roll greater than 1°). After

TABLE 1. Overview of conditions during the selected three 15-min segments of the dataset. Here, H_s is the significant wave height; T_m and T_p are the mean and peak wave periods, respectively; W_{20m} is the wind speed at 20-m height; N_{15m} is the buoyancy frequency at 15-m depth; L_O is the Ozmidov length scale; u is the flow along the axis of the instrument; AOA is the angle of attack; and ε is the dissipation rate of TKE.

		1	2	3
Date	(2011)	10 Apr	12 Apr	12 Apr
Time	(UTC)	1440	0000	2000
H_s	(m)	2.0	1.0	0.9
T_m	(s)	5.3	4.7	7.1
T_p	(s)	7.7	7.9	13.0
W_{20m}	($m\,s^{-1}$)	13.5	0.7	11.0
N_{15m}	(s^{-1})	2.9×10^{-3}	5.3×10^{-3}	8.9×10^{-3}
L_O	(m)	7.8	0.2	0.6
u	($cm\,s^{-1}$)	17 ± 3	17 ± 2	18 ± 3
AOA	(°)	2.1 ± 0.4	2.3 ± 0.4	1.5 ± 0.3
ε	($W\,kg^{-1}$)	1.5×10^{-6}	8.4×10^{-9}	2.2×10^{-7}

data screening, 46% of the data are available for the analysis.

5. Results and discussion

a. Spectra

Three 15-min segments are chosen (Table 1) when 1) the conditions were windy with large significant wave height H_s, 2) calm with small H_s, and 3) windy with small waves with a longer period. The average dissipation rate between each 15-min segment varied by almost three orders of magnitude spanning 8.4×10^{-9} to $1.5 \times 10^{-6}\,W\,kg^{-1}$. The number of 60-s segments that satisfied the criteria for quality screening for shear spectra were 5, 10, and 25, respectively. In all cases AOA_{HF} was approximately 2°. The spectra are calculated from each 15-min segment using half-overlapping 128-s (2.13 min) segments, in order to show the relatively low-frequency portion covering the wave band.

Figure 8 shows the spectra inferred from the motion sensor using complementary filtering of the linear and rotation rate sensors. The inertial acceleration dominates the low-frequency motion. In general, the axial component is the most energetic at low frequencies ($f <$ 0.2 Hz). Toward the high-frequency end of the surface wave band, the lateral motion dominates. The most energetic motions are seen during period 1 with strong wind and large wave height. In the frequency range 1–20 Hz chosen for dissipation rate calculations, acceleration spectra are near the noise level.

The velocity spectra from the ADV Vector are entirely dominated by the wave orbital velocities and approach the noise level at 0.3–0.5 Hz (Fig. 9). Because of

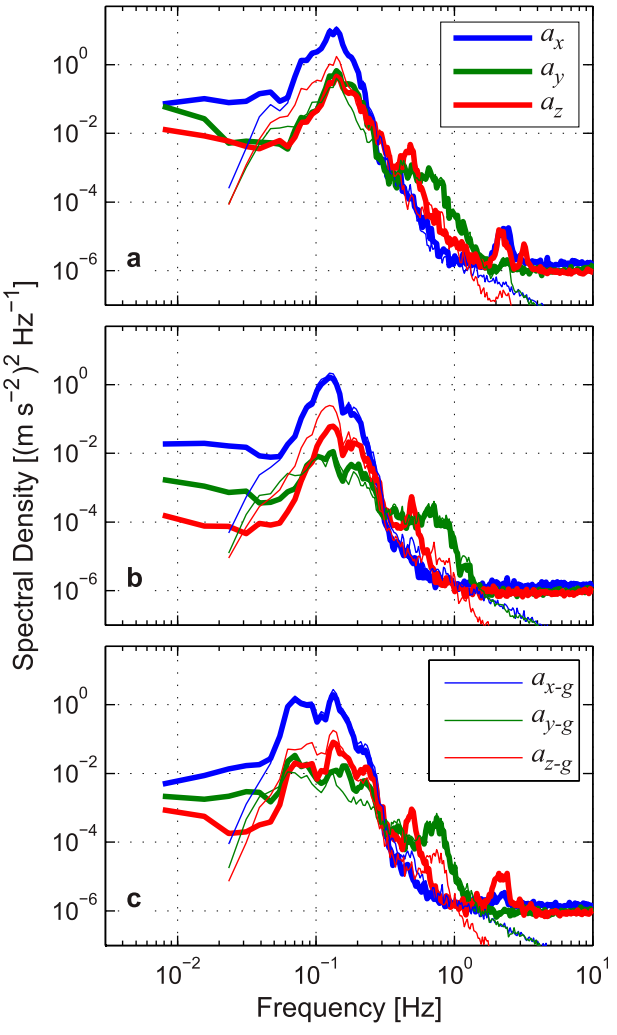

FIG. 8. Frequency spectra from the motion sensor (gyro) for the three selected periods: (a) 1, (b) 2, and (c) 3, marked in Fig. 4. Half-overlapping 128-s segments are used to produce the spectra that are then band averaged at $\log_{10}(\Delta f) = 0.01$ intervals. Spectra are shown from the components of linear acceleration (thick) and the gravitational components (thin lines) inferred from complementary filtering of the linear and rotation rate sensors with a cutoff period of 25 s.

the configuration of the acoustic beams, the axial component has a lower noise level. No credible near-inertial subrange can be detected; the spectra are contaminated by the wave band in the low-frequency portion and noise in the high-frequency portion. It is therefore not possible to utilize the ADV data for dissipation rate estimates or eddy-covariance calculations. Although the motion correction can be attempted using the six-axis motion sensor (see, e.g., Perlin and Moum 2012), the portion of the spectra above the noise level is so narrow ($f <$ 0.3 Hz) that the inertial band cannot be recovered with confidence. We only concentrate on the shear probe

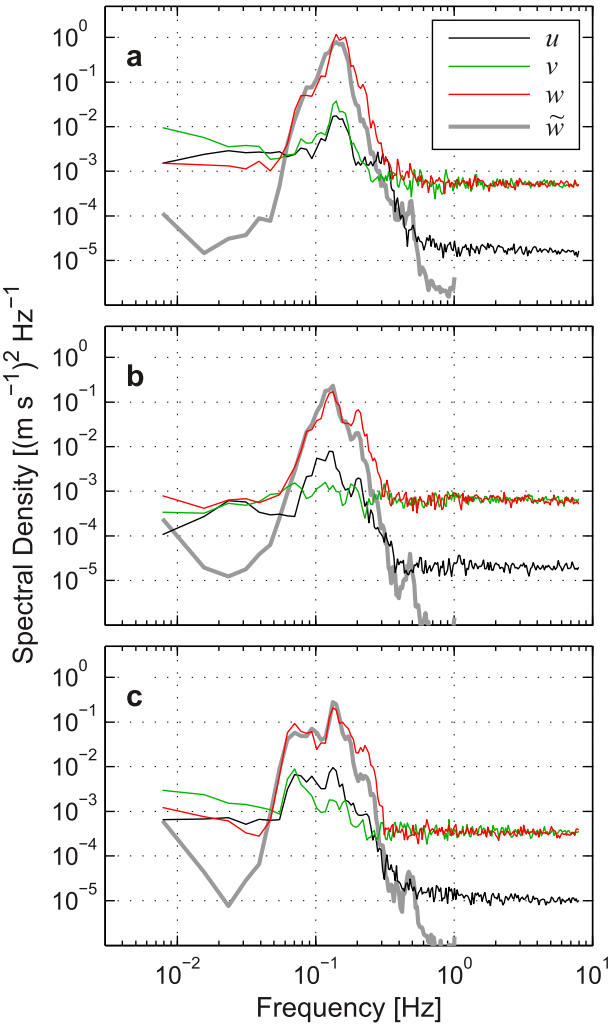

FIG. 9. As in Fig. 8, but for the u, v, and w components of the velocity measured by the Vector. Segmenting and band averaging as in Fig. 8. Also shown are the spectra of the wave orbital velocity $\tilde{w}$ (gray) at the measurement depth, inferred from motion-corrected pressure time series using the linear wave theory.

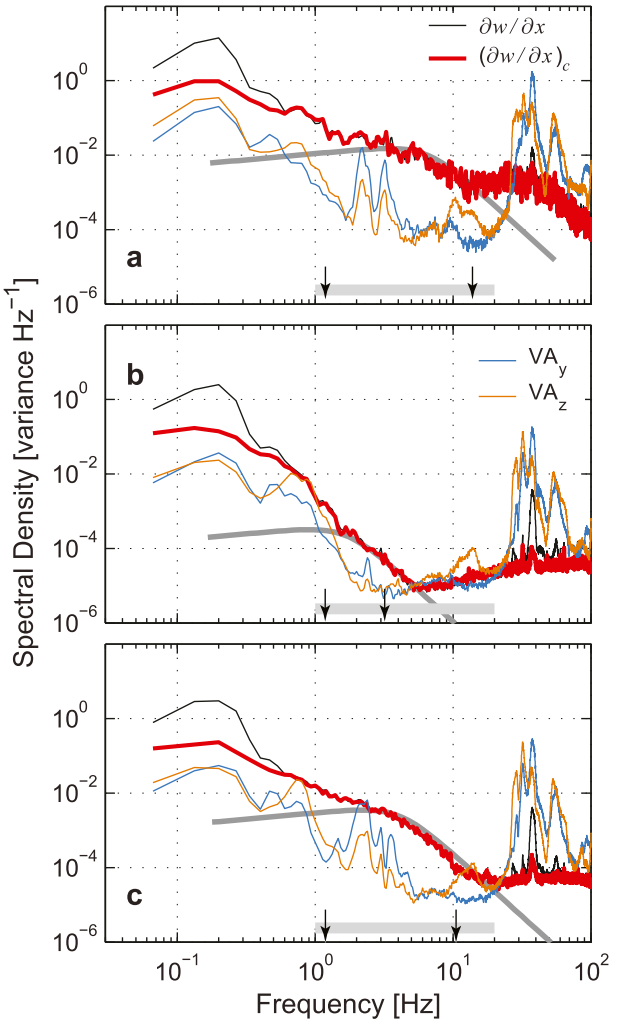

FIG. 10. As in Fig. 8, but for turbulence shear $\partial w/\partial x$ (black) and the two components of the piezo-accelerometers (vibration sensors), VA$_y$ and VA$_z$. The thick red curves are the clean shear spectra after removing the parts of the signal coherent with the accelerometers $(\partial w/\partial x)_c$. Nasmyth's turbulence spectrum for the inferred average ε is shown by gray curves. The horizontal gray band shows the range of the spectra extracted for calculation of the dissipation rate. Note that this is not the integration band over which the shear variance is calculated, but it is the portion of the spectrum passed on to the routine that iteratively adjusts the integration band. Correction for the lost variance is a factor of 1.7 for periods 1 and 3 and 2 for period 2. Integration wavenumber band (arrows) is 4–50, 6–16, and 5–47 cpm. The number of 60-s segments that were averaged is 5, 10, and 25.

data at high frequencies uncontaminated by the surface gravity wave band. Because the instrument is moored, it responds relatively easily to horizontal motions than the vertical motions, absorbing a large fraction of the wave band variance in the horizontal components.

The shear spectra for the three selected periods are shown in Fig. 10, together with the spectra from the vibration sensors (piezo-accelerometers). Note that the spectral levels obtained from the vibration sensors are arbitrary (vibration sensors are not calibrated), and are only used to identify and remove the shear spectral variance coherent with the vibrations. For decontamination of the shear signals using the Goodman et al. (2006) method, a signal in physical units is not required. The average spectra from the first period are relatively noisy as only five spectra are ensemble averaged. Both components of the acceleration show elevated levels of vibration at high frequencies (>20 Hz), comparable to those in $f < 1$ Hz, covering the wave band. The frequency band between 1 and 20 Hz is relatively unaffected by wave motions or vibrations and is chosen for calculation of the dissipation rate. There are narrowband

peaks in the vibration spectra in this band; however, the shear spectral levels are either high, unaffected by them, or are satisfactorily cleaned using the Goodman et al. (2006) method. In a fraction of the identified clean frequency band, the shear spectra conform to the empirical shape of the Nasmyth spectrum shown by the gray curves.

In stratified flows, a transition subrange exists between the internal gravity waves and the inertial subrange. This buoyancy subrange is associated with the intermediate range of scales larger than those in the inertial subrange. An analytical theory of the buoyancy–inertial subrange transition in turbulent flows with stable stratification has recently been presented in Sukoriansky and Galperin (2012), who also obtain theoretical expressions for kinetic energy and shear spectra, normalized by the Ozmidov length scale. The Ozmidov length scale, $L_O = (\varepsilon N^{-3})^{1/2}$, is one of the most important scales of stratified turbulence; L_O delineates the scale at which the turbulence eddy turnover time is equal to the time scale of internal wave in a stratified flow. Hence, it is a measure of the maximum vertical overturn displacement that may occur. Our measurements were made in the upper, quasi-mixed layer where the stratification was typically not different from zero to within the measurement uncertainty of the SBE MicroCAT sensors. For a typical density measurement error of 0.01 kg m^{-3}, and using the vertical separation of 6 m of the SBE instruments, the noise level is $N^2 \sim 1.6 \times 10^{-5}\,\mathrm{s}^{-2}$ or $N \sim 4 \times 10^{-3}\,\mathrm{s}^{-1}$. The calculation of N is detailed in section 5f, where a time series is also presented. The average values of N and L_O for the three chosen segments are given in Table 1; N is close to or below the noise level for the first two segments, and it is only a factor of 2 larger in segment 3. While we cannot test the applicability of Sukoriansky and Galperin (2012) in our dataset, deployments of MATS in stratified flow and away from the wave-affected layer may be utilized to test this fundamental theory against the observations.

b. Wave orbital velocities

According to the linear wave theory, the horizontal and vertical components of wave orbital velocities at depth z are given by

$$\tilde{u}(z,t) = \sum_{m=1}^{n} \sigma_m \frac{\cosh[k_m(z+d)]}{\cosh(k_m d)} \eta_m(t) \qquad (6)$$

and

$$\tilde{w}(z,t) = \sum_{m=1}^{n} \sigma_m \frac{\sinh[k_m(z+d)]}{\sinh(k_m d)} \tanh(\sigma_m t)\eta_m(t), \qquad (7)$$

where d is the total water depth, index m is the mth component of sinusoidal wave, and n denotes the total number of wave components. In the absence of Doppler shifting of (radian) wavenumber k, the (radian) frequency σ is prescribed by the dispersion relation $\sigma^2 = gk\tanh(kd)$, and $\eta = a\cos(-\sigma t + \phi)$ is the sinusoidal wave surface displacement with amplitude a and random phase ϕ.

In Fig. 9 the frequency spectra of the inferred wave orbital velocity $\tilde{w}$ at the measurement depth are compared to the velocity spectra from the Vector records. The spectra of the horizontal components of the wave orbital velocity are approximately equal to the spectra of $\tilde{w}$ and are not shown. The variance in the 0.05–0.3-Hz frequency range is entirely associated with the wave orbital velocities. The variance in the horizontal components is suppressed primarily due to the motion of the platform, which can relatively easily respond to the flow—hence, absorb the oscillations—in the horizontal rather than in the vertical.

c. Flow distortion

As the free streamflow approaches the instrument, flow distortion occurs, both because of the platform body and the sensors. The flow distortion modifies the vorticity and the velocity fields near the sensors. Wyngaard et al. (1985) derive errors associated with turbulence measurements from an axisymmetric body. Errors depend on the flow distortion matrix, which includes five independent elements of distortion coefficients, which relate the velocity near the body to the free stream velocity. For axisymmetric bodies off-diagonal coefficients vanish on the long axis of the body, and errors depend only weakly on AOA (Wyngaard et al. 1985). Their example of an ellipsoid of revolution with an aspect ratio, L/D, of 5:1, where D is the maximum diameter of the body and L is its length, is comparable to the MATS platform ($L = 3$ m, $D = 0.46$ m, and an aspect ratio of 6.5:1). The sensors are at a plane 0.55 D (shear probes) and 0.65 D (Vector) ahead of the nose of the buoy, and are located approximately at the long axis of the body. For a 5:1 ellipsoid, measurements at a plane 0.5 D ahead of the body, along the axis, Wyngaard et al. (1985) found that the fractional errors in turbulent velocity statistics are on the order of 10%. Osborn and Lueck (1985) conducted turbulence measurements using shear probes and FP07 thermistors from a research submarine ($L = 51$ m and $D = 5.6$ m) and placed the sensors approximately 0.88 D atop the main body of the submarine. They discussed the flow distortion about the hull and the sensor mount and found it to be negligible. Furthermore, the nose of the buoy, the MicroRider, and the shear probes are all

tapered to reduce the local diameter and the associated flow distortion. At the nose, the buoy diameter is 15 cm, yielding measurements at approximately two diameters away from the body. Overall, we conclude that the effect of flow distortion is negligible relative to other potential sources of errors and noise associated with the measurements.

d. Noise level for shear measurements

The measurements were made in the wave-affected layer where the dissipation levels were large. The dataset is therefore not ideal to estimate the noise level for the shear probe measurements. The 2-s low-pass filtered flow is used to convert the raw (output of the analog-to-digital converter) shear probe signal into physical units, and then into the wavenumber domain. For a given noise spectrum, this conversion will determine the lowest detection level of the dissipation rate; the noise level increases for slow mean flow. We infer the electronic noise spectrum from a bench test in the laboratory using open circuit dummy probes, and the shear probe noise spectrum by selecting quiescent segments from the deployment when the instrument is affected by the environment. To select quiescent segments from the dataset, the frequency spectra are calculated using unit mean flow, to get the variance independent of the flow, from the raw shear data in counts. The variance between 1 and 5 Hz is obtained by integrating each spectrum. The lowest 2.5 percentile—a total of 199 segments, each lasting for 60 s—are chosen to characterize the noise spectrum. Note, however, that the near-surface layer is turbulent and the most quiescent shear spectra may not be representative of a possibly lower detection level. The average raw frequency spectra are shown in Fig. 11a for shear probes 1 ($\partial w/\partial x$) and 2 ($\partial v/\partial x$), together with the minimum and maximum envelope of the 199 spectra for $\partial w/\partial x$. The spectra are band averaged in frequency in 60 logarithmically equally spaced bins. Also shown is the electronic noise spectrum, not bin averaged, for the shear probe 1 channel, using a dummy probe (that from the second probe channel is nearly identical and is not shown). Clearly, the environmental factors affect the noise spectrum. The system's endemic vibration noise, resulting from environmental and mechanical factors, is amplified by the shear probe differentiation. The white, low-frequency portion of the bench spectrum is elevated by more than five orders of magnitude in the surface gravity wave band, abruptly falling to low levels between 0.5 and 4 Hz, before slowly increasing with frequency due to electronic noise. The shape of the noise spectrum at high frequencies is similar to that of the bench spectrum, but with values a factor of 10 larger. These spectra can be compared to Fig. 10 of Lueck et al. (1997), which shows similar structure at high frequencies but with the levels at 0.1 Hz three decades lower. The difference can almost entirely be attributed to the contamination by surface waves.

The noise spectra from probe 1 are converted into equivalent shear wavenumber spectra for $\partial w/\partial x$ in Fig. 11b using various mean flow speeds. When the mean flow is $10\,\mathrm{cm\,s^{-1}}$, the noise level in terms of the dissipation rate reaches $3 \times 10^{-8}\,\mathrm{W\,kg^{-1}}$. For a flow of $25\,\mathrm{cm\,s^{-1}}$, representative of the observations, $\varepsilon \approx 10^{-9}\,\mathrm{W\,kg^{-1}}$ can be resolved. Because the typical dissipation levels in the upper surface layer are large, this level of noise is acceptable. However, for deployments in relatively quiescent waters, a stronger mean flow is needed in order to resolve smaller dissipation rates. The part of the noise spectrum decaying rapidly from the wave frequencies to the dissipation subrange dwarfs the near-inertial subrange of the Nasmyth spectrum (the relatively white low wavenumber part), and typically contaminates the wavenumbers until the empirical shear spectrum rolls off.

e. Dissipation-binned shear spectra

Shear spectra from the 60-s segments satisfying the quality screening are averaged in bins of dissipation rate between 10^{-9} and $10^{-5}\,\mathrm{W\,kg^{-1}}$. The frequency domain and wavenumber domain spectra are shown separately for $\partial w/\partial x$ in Fig. 12. The variance of shear coherent with accelerometers is successfully removed (cf. the raw and clean spectra) in the surface gravity wave band, for narrowband vibrations at about 2 Hz when ε was small, and partly for vibrations at high frequencies, which are out of the frequency range chosen for dissipation rate calculations. The corresponding (clean) wavenumber spectra typically follow Nasmyth's shape after the roll off. In the near-inertial subrange of Nasmyth's curve, on the low wavenumber part of the spectrum before the roll off, the observed shear spectra are contaminated by the variance decay from the wave band, resembling the shape in the noise spectrum. This can be partly eliminated by, for example, removing the corresponding noise spectrum for the segment-mean flow, from each 60-s shear spectrum. This is not attempted here. Alternatively, we can constrain the low wavenumber cutoff of the integration band, for the dissipation rate calculation in Eq. (2), to increasingly large values for increasing dissipation rates. Because the lower wavenumber cutoff typically is between 4 and 6 cpm in our processing, the dissipation rate estimates for $\varepsilon > 10^{-8}\,\mathrm{W\,kg^{-1}}$ are about a factor of 2 larger than those inferred from Nasmyth's spectrum, which fit best to the portion after the spectral roll off (cf. the empirical and observed curves in Fig. 12b).

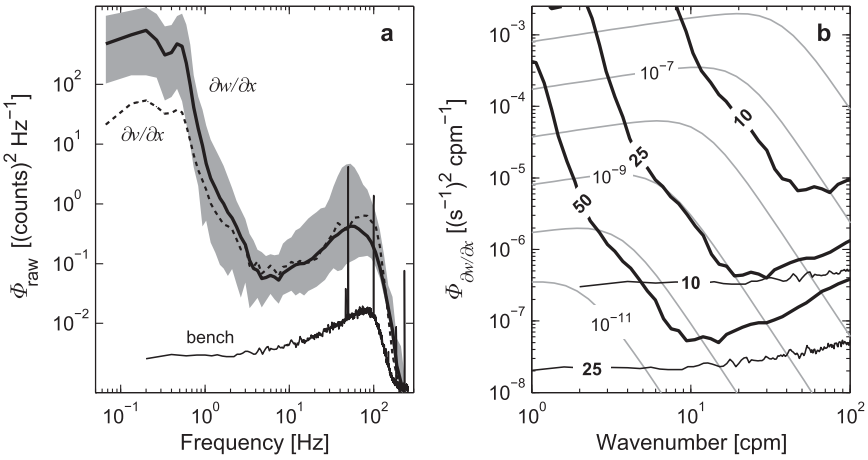

FIG. 11. Noise spectra for shear. (a) Frequency spectra of the raw output of the shear probes averaged for 199 segments, each lasting 60 s, when the shear variance was low. The thick black line is the spectrum from shear probe 1 ($\partial w/\partial x$) with gray-shaded region indicating the minimum and maximum ranges; the dashed line is the mean spectrum from shear probe 2 ($\partial v/\partial x$). Average spectra are band averaged in frequency in 60 logarithmically equally spaced bins. Spectrum from a 15-min-long record from a bench test in the laboratory using an open-circuit dummy probe is also shown as reference for the electronic noise. (b) Noise spectra inferred from quiescent shear spectra (thick curves) converted into physical units, and into wavenumber spectra, using a mean flow increasing from 10 to 50 cm s^{-1}. Gray curves are the spectral shapes after Nasmyth for ε of 10^{-6} to 10^{-11} W kg^{-1}. Corresponding electronic noise spectrum from the bench test (thin lines) is also shown for a mean flow of 10 and 25 cm s^{-1}.

We speculate that the spectral shape in this frequency range is induced by unsteady advection of shear variance due to wave orbital velocities, in a similar manner as described in Lumley and Terray (1983). While methods exist for evaluating these effects in the presence of unidirectional (e.g., Trowbridge and Elgar 2001) or multidirectional waves (Gerbi et al. 2009), it is not the scope of the present work to further investigate this

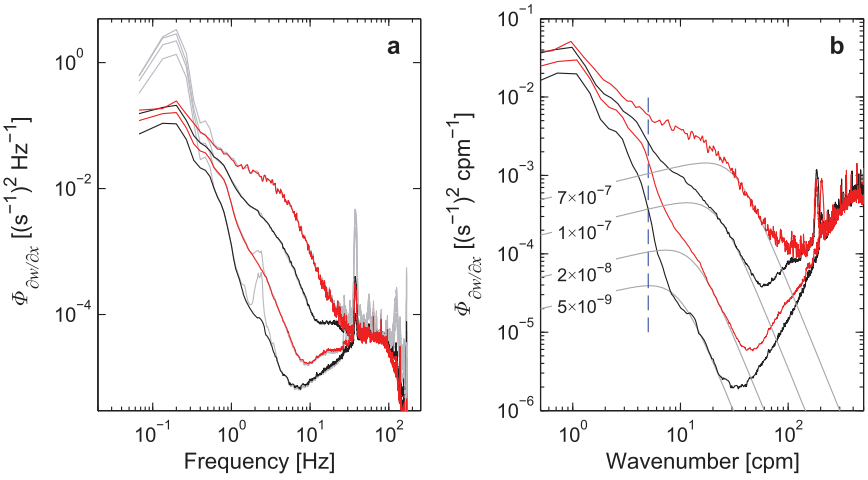

FIG. 12. Shear spectra averaged in decadal increment bins of dissipation rate between 10^{-9} and 10^{-5} W kg^{-1} (a) original (gray) and cleaned (alternating black and red) frequency spectra of $\partial w/\partial x$. The number of spectra averaged is 344, 1386, 1427, and 64, respectively, from the lowest to the highest ε. (b) The corresponding (clean) wavenumber spectra. The gray curves are the spectral shapes after Nasmyth for indicated ε (W kg^{-1}). The ε averaged over the corresponding segments are 5×10^{-9}, 4×10^{-8}, 2.8×10^{-7}, and 1.3×10^{-6} W kg^{-1}. Vertical dashed line marks 6 cpm for reference.

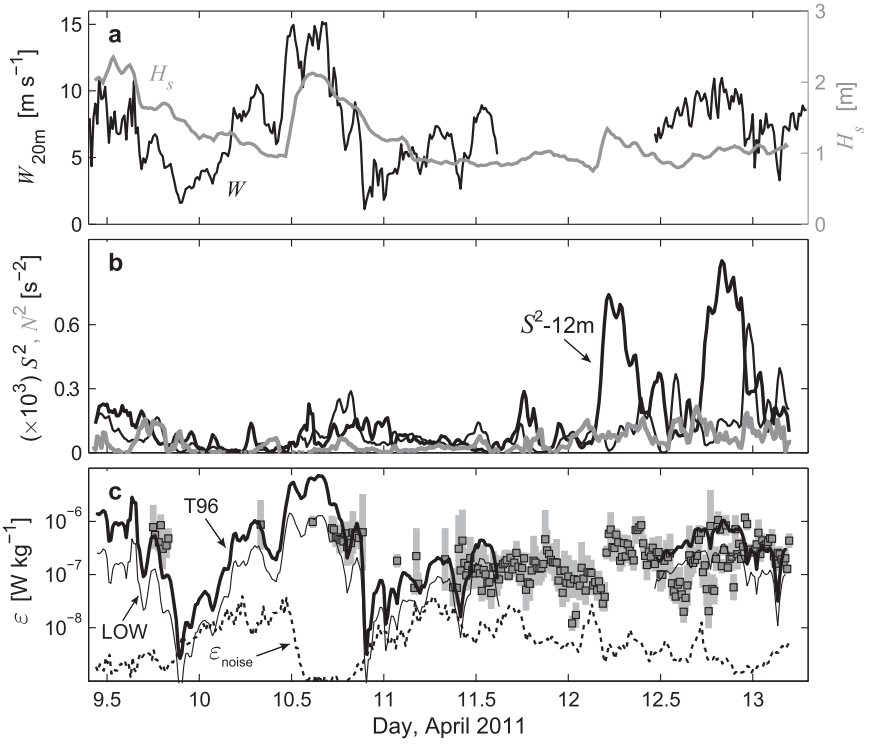

FIG. 13. Time series of measured dissipation rate of TKE, ε. Selected environmental forcing parameters are also shown for reference. (a) Wind speed W_{20m} and significant wave height H_s as in Fig. 7. (b) Shear-squared (black) and buoyancy frequency squared (gray), 4-m first difference inferred between bins at 10 and 14 m (S^2-12m), and 6-m first difference between 12 and 18 m, where joint velocity and density measurements are available (thin black, S^2-15m, and gray, N^2-15m). (c) Dissipation rate, 15-min averages, and 95% confidence intervals (markers and gray bars). Thick black line marked T96 is the ε predicted by the Terray et al. (1996) scaling [Eq. (8)]. Thin line indicates the dissipation expected from LOW. Wind speed measurements and friction velocity (hence wind speed) dependent T96 and LOW during the period when the ship was moored near land are excluded. The dashed curve is the lowest detection level of dissipation rate ε_{noise} estimated as a function of the mean flow.

point. It is, however, expected that high-quality shear spectra can be obtained in the absence of oscillatory high-frequency (1–10-s period) flow.

f. Dissipation rate time series

Time series of measured dissipation rate ε are obtained using the 60-s values that satisfied the quality control criteria (section 5d). The record is averaged in 15-min segments using the maximum likelihood estimator from a lognormal distribution (Baker and Gibson 1987). At least four data points are required in each 15-min bin. The results are shown in Fig. 13, together with the 95% confidence limits and selected environmental forcing parameters. A simple arithmetic averaging produces comparable results. Unfortunately, in the early half of the record, the mean flow is weak, resulting in small R and large AOA, hence a substantial loss of data.

Using identical methods to dissipation rate calculations from shear spectra, we calculate ε from the noise spectra (section 5d) for a mean flow varying between 5 and 80 cm s^{-1}, at 5 cm s^{-1} increments. An estimate of the lowest detection level for the dissipation rate (ε_{noise}) as a function of the mean flow is then obtained by a fourth-order polynomial fit. A time series for the noise level is then estimated using this function and the flow speed at each 15-min segment and is shown in Fig. 13c by the dashed curve. Measured ε is above the noise level at all times.

MATS is located in the wave-affected surface layer; the dissipation rate is expected to be largely a result of breaking waves, particularly in wavy conditions. Lacking independent measurements of dissipation rate for ground truthing our ε time series, we turn to a widely used parameterization for the dissipation expected for deep-water wave breaking (Terray et al. 1996) in order

to test and interpret our results. The Terray et al. (1996) scaling is

$$\frac{\varepsilon H_s}{F_k} = 0.3\left(\frac{z}{H_s}\right)^{-2}, \tag{8}$$

where $F_k = \beta(u_*)^3$ is the breaking-wave-induced flux of TKE into the water column; u_* is the water-side friction velocity; and β is a wave parameter dependent on the wave age, the phase speed of waves, and the air-side friction velocity. However, β is not well constrained and varies between about 90 and 250 (Terray et al. 1996; Gerbi et al. 2009). Resulting ε using $\beta = 250$ at $z = 12$ m and H_s inferred from MATS is compared to the observed dissipation rates (Fig. 13c). It is not the aim of this study to tune the constant β or to verify the applicability of this scaling; the scaling is merely used to show that the dissipation rates measured by MATS are in the expected range and show a time evolution consistent with the forcing. Because our dissipation rates are about a factor of 2 overestimated for these large values of ε (section 5e), β used here is likely an overestimate accordingly. Overall, when the background shear in the measurement level is not elevated relative to the stratification, there is a broad agreement between the measured ε and that expected from the Terray et al. (1996) scaling. For reference, we also show the dissipation rate expected from the law of the wall (LOW), $\varepsilon = (u_*)^3/0.4z$, which may be relevant at the measurement depth of order $10H_s$.

Joint velocity and density measurements are available from the ADCP bins and MicroCATs at 12 and 18 m. The shear squared (S^2) and buoyancy frequency squared (N^2) centered at 15-m depth, about 3 m below the MATS, are calculated using 6-m first differencing (shown by thin black and gray lines, respectively, in Fig. 13b). Additionally, velocity measurements from bins at 10 and 14 m are used to calculate the shear squared at 12 m—that is, at the level of MATS (S^2-12m, thick line). When there are large discrepancies from the Terray scaling, S^2-12m is large. Unfortunately, wind measurements are not available, representative of the measurement site, when the ship was moored near land between late 11 April and early 12 April. Averaged over 3 h centered at 1800 UTC 11 April, and 0500 and 2000 UTC 12 April, N^2-15m/S^2-12m is 0.05, 0.13, and 0.07, respectively—that is, significantly less than unity. Assuming that N^2 at 15 m calculated over a 6-m vertical length is representative of N^2 at 12 m calculated over a 4-m vertical length, this ratio is an approximation to the gradient Richardson number. Enhanced production of TKE by background shear can thus be expected, a mechanism not accounted for in the scaling in Eq. (8).

6. Conclusions

A moored, self-recording turbulence instrument was successfully deployed in 128 m water at 12 m from the surface in the wave-affected boundary layer. It is demonstrated that the time series of the dissipation rate of TKE can be collected, at a fixed level, for an extended period of time, using shear probes. In the wave-affected layer, the quality of the measurements is constrained by the angle of attack (AOA) and the magnitude of mean flow relative to the wave oscillatory velocities. In the present experiment, the flow is not sufficiently stronger than the wave-induced motion for 54% of the duration, leading to a significant reduction in high-quality data return. The instrument, otherwise, is very stable and is capable of making high-quality dissipation measurements in the water column (away from the wave boundary layer) given strong enough mean flow to advect turbulent eddies past the sensors. A recent deployment made in the turbulent Faroe Bank Channel overflow interface (I. Fer 2014, unpublished manuscript) produced a high-quality dissipation rate time series. The presence of an ADV, rigidly fixed to the platform, sampling the 3D velocity, particularly the component oriented along the axis of the instrument, is crucial for converting the shear probe output to physical shear and for estimating the AOA. When strong axial flows are anticipated (e.g., $>1\,\mathrm{m\,s^{-1}}$), caution is advised to avoid possible phase wrapping by the Doppler velocimeter.

The shape of the shear spectra, collected in the wave-affected layer by MATS, comprises an energetic low-frequency portion (0.05–1 Hz) directly affected by surface gravity waves, a transition region (1–3 Hz) likely affected by the unsteady advection due to surface waves, and the dissipation range of the spectrum (3–20 Hz) after the spectrum starts to roll off. Vibration noise dominates the higher frequencies. The shear spectra are found to be relatively free of contamination by wave affects or body-induced motions in the 1–20-Hz frequency range, which is further used for dissipation rate calculations. For a weak mean flow of $10\,\mathrm{cm\,s^{-1}}$, the noise level in terms of the dissipation rate reaches $3 \times 10^{-8}\,\mathrm{W\,kg^{-1}}$. For a flow of $25\,\mathrm{cm\,s^{-1}}$, $\varepsilon \approx 10^{-9}\,\mathrm{W\,kg^{-1}}$ can be resolved. Because the typical dissipation levels in the upper surface layer are large, this level of noise is acceptable. However, for deployments in relatively quiescent waters, stronger mean flow is needed in order to resolve smaller dissipation rates.

The resulting time series of the dissipation rate shows a variability of three orders of magnitude. The sampling in time allows for calculations in 60-s segments, which is a step further in adequately resolving and sufficiently averaging the intermittency, which is not possible using

profiling instruments. The evolution of the dissipation rate in time is consistent with forcing mechanisms: there is a broad agreement between the measured ε and that expected from breaking waves, and the dissipation is elevated when the background shear favors TKE production by mean shear.

Acknowledgments. This work was funded by the Norwegian Centre for Offshore Wind Energy (NORCOWE) under Grant 193861/S60 from the Research Council of Norway. The authors thank Rolf Lueck for the valuable discussions, and Kai Christensen and Svein Sundby for making it possible to deploy MATS during a BIOWAVE cruise, and three reviewers for their insightful comments.

REFERENCES

Baker, M. A., and C. H. Gibson, 1987: Sampling turbulence in the stratified ocean: Statistical consequences of strong intermittency. *J. Phys. Oceanogr.,* **17,** 1817–1836.

Bakhoday Paskyabi, M., and I. Fer, 2013: Turbulence measurements in shallow water from a subsurface moored moving platform. *Energy Procedia,* **35,** 307–316, doi:10.1016/j.egypro.2013.07.183.

Edson, J. B., A. A. Hinton, K. E. Prada, J. E. Hare, and C. W. Fairall, 1998: Direct covariance flux estimates from mobile platforms at sea. *J. Atmos. Oceanic Technol.,* **15,** 547–562.

Fer, I., and K. Widell, 2007: Early spring turbulent mixing in an ice-covered Arctic fjord during transition to melting. *Cont. Shelf Res.,* **27,** 1980–1999.

Gerbi, G. P., J. H. Trowbridge, E. A. Terray, A. J. Plueddemann, and T. Kukulka, 2009: Observations of turbulence in the ocean surface boundary layer: Energetics and transport. *J. Phys. Oceanogr.,* **39,** 1077–1096.

Goodman, L., E. R. Levine, and R. G. Lueck, 2006: On measuring the terms of the turbulent kinetic energy budget from an AUV. *J. Atmos. Oceanic Technol.,* **23,** 977–990.

Lueck, R. G., D. Huang, D. Newman, and J. Box, 1997: Turbulence measurement with a moored instrument. *J. Atmos. Oceanic Technol.,* **14,** 143–161.

——, F. Wolk, and H. Yamazaki, 2002: Oceanic velocity microstructure measurements in the 20th century. *J. Oceanogr.,* **58,** 153–174.

Lumley, J. L., and E. A. Terray, 1983: Kinematics of turbulence convected by a random wave field. *J. Phys. Oceanogr.,* **13,** 2000–2007.

McPhee, M. G., 1992: Turbulent heat flux in the upper ocean under sea ice. *J. Geophys. Res.,* **97** (C4), 5365–5379.

——, 2008: *Air–Ice–Ocean Interaction: Turbulent Ocean Boundary Layer Exchange Processes.* Springer, 215 pp.

——, G. A. Maykut, and J. H. Morison, 1987: Dynamics and thermodynamics of the ice/upper ocean system in the marginal ice zone of the Greenland Sea. *J. Geophys. Res.,* **92** (C7), 7017–7031.

Moum, J. N., and J. D. Nash, 2009: Mixing measurements on an equatorial ocean mooring. *J. Atmos. Oceanic Technol.,* **26,** 317–336.

——, M. C. Gregg, R. C. Lien, and M. E. Carr, 1995: Comparison of turbulent kinetic energy dissipation rate estimates from two ocean microstructure profilers. *J. Atmos. Oceanic Technol.,* **12,** 346–366.

Mudge, T. D., and R. G. Lueck, 1994: Digital signal processing to enhance oceanographic observations. *J. Atmos. Oceanic Technol.,* **11,** 825–836.

Osborn, T. R., and C. W. Crawford, 1980: An airfoil probe for measuring turbulent velocity fluctuations in water. *Air–Sea Interactions: Instruments and Methods,* F. Dobson, L. Hasse, and R. Davis, Eds., Plenum Press, 369–386.

——, and R. G. Lueck, 1985: Turbulence measurements with a submarine. *J. Phys. Oceanogr.,* **15,** 1502–1520.

Perlin, A., and J. N. Moum, 2012: Comparison of thermal variance dissipation rates from moored and profiling instruments at the equator. *J. Atmos. Oceanic Technol.,* **29,** 1347–1362.

Röhrs, J., K. H. Christensen, L. R. Hole, G. Broström, M. Drivdal, and S. Sundby, 2012: Observation-based evaluation of surface wave effects on currents and trajectory forecasts. *Ocean Dyn.,* **62,** 1519–1533.

Sukoriansky, S., and B. Galperin, 2012: An analytical theory of the buoyancy–Kolmogorov subrange transition in turbulent flows with stable stratification. *Philos. Trans. Roy. Soc. London,* **371A,** 20120212, doi:10.1098/rsta.2012.0212.

Terray, E. A., M. A. Donelan, Y. C. Agrawal, W. M. Drennan, K. K. Kahma, A. J. Williams, P. A. Hwang, and S. A. Kitaigorodskii, 1996: Estimates of kinetic energy dissipation under breaking waves. *J. Phys. Oceanogr.,* **26,** 792–807.

Thorpe, S. A., 2005: *The Turbulent Ocean.* Cambridge University Press, 439 pp.

Trowbridge, J., and S. Elgar, 2001: Turbulence measurements in the surf zone. *J. Phys. Oceanogr.,* **31,** 2403–2417.

Wunsch, C., and R. Ferrari, 2004: Vertical mixing, energy, and the general circulation of the oceans. *Annu. Rev. Fluid Mech.,* **36,** 281–314.

Wyngaard, J. C., L. Rockwell, and C. A. Friehe, 1985: Errors in the measurement of turbulence upstream of an axisymmetric body. *J. Atmos. Oceanic Technol.,* **2,** 605–614.

Zhang, Y., and J. N. Moum, 2010: Inertial-convective subrange estimates of thermal variance dissipation rate from moored temperature measurements. *J. Atmos. Oceanic Technol.,* **27,** 1950–1959.